Unlocking the Second Electron in the Electrochemical Delithiation/Lithiation of Copper (2,5-Dilithium-oxy)-Terephthalate via a Carbon-Supported Electrode Architecture

Aswadh Shyma Sajeevan, Daniel Brandell, Philippe Moreau, Stéven Renault, Philippe Poizot

▶ **To cite this version:**

Aswadh Shyma Sajeevan, Daniel Brandell, Philippe Moreau, Stéven Renault, Philippe Poizot. Unlocking the Second Electron in the Electrochemical Delithiation/Lithiation of Copper (2,5-Dilithium-oxy)-Terephthalate via a Carbon-Supported Electrode Architecture. ChemSusChem, inPress, ⟨10.1002/cssc.202501002⟩. ⟨hal-05296731⟩

HAL Id: hal-05296731

https://hal.science/hal-05296731v1

Submitted on 6 Oct 2025

HAL is a multi-disciplinary open access archive for the deposit and dissemination of scientific research documents, whether they are published or not. The documents may come from teaching and research institutions in France or abroad, or from public or private research centers.

L'archive ouverte pluridisciplinaire **HAL**, est destinée au dépôt et à la diffusion de documents scientifiques de niveau recherche, publiés ou non, émanant des établissements d'enseignement et de recherche français ou étrangers, des laboratoires publics ou privés.

HAL Authorization

Unlocking the Second Electron in the Electrochemical Delithiation/Lithiation of Copper (2,5-Dilithium-oxy)-Terephthalate via a Carbon-Supported Electrode Architecture

Aswadh Shyma Sajeevan,[a, b] Daniel Brandell,[c] Philippe Moreau,[a] Stéven Renault,*[a] and Philippe Poizot*[a]

[a]Department of Chemistry
Nantes Université, CNRS, Institut des Matériaux de Nantes Jean Rouxel
F-44000 Nantes, France
E-mail: Steven.Renault@cnrs-imn.fr, Philippe.Poizot@cnrs-imn.fr

[b]ALISTORE-European Research Institute

[c]Department of Chemistry−Ångström Laboratory, Uppsala University
SE-751 21 Uppsala, Sweden

Supporting information for this article is given via a link at the end of the document.

Abstract: Copper (2,5-dilithium-oxy)-terephthalate (Cu(Li_2)-*p*-DHT) was synthesized and thoroughly characterized using a range of analytical techniques, then evaluated electrochemically as a lithiated host material for positive electrodes in Li half-cells. When formulated as a carbon-supported organic electrode material, the compound reaches its full theoretical two-electron capacity, delivering a specific capacity of 188.2 mAh g^{-1}, almost double that of previously reported M(Li_2)-*p*-DHT analogues (~100 mAh g^{-1}). However, its cycling stability remains limited due to the formation of a fully oxidized quinone species in the delithiated state, as evidenced by FTIR spectroscopy. This oxidized form was found partially soluble in carbonate-based electrolytes, resulting in poor cycling performance. By narrowing the potential window to the one-electron storage reaction, cycling performance improves significantly, with 96 % capacity retention after 50 cycles and a coulombic efficiency exceeding 99 %, albeit at a reduced capacity of ~80 mAh g^{-1}. Electron energy loss spectroscopy (EELS) further confirmed the gradual structural evolution from the semiquinone to quinone form. These

results highlight key design principles for enhancing lithium extraction in lithiated organic host materials and represent a significant step toward achieving capacities that approach those of conventional inorganic electrodes.

Introduction

Lithium-ion batteries (LIBs) currently dominate the energy storage landscape ranging from portable electronics to large-scale stationary systems due to their well-established advantages in energy density and cycle life.[1–4] However, their production and end-of-life management raise critical environmental concerns, which are further exacerbated by limited recycling infrastructure and low material recovery rates. As LIBs demand continues to grow in line with the global push for widespread electrification, large volumes of spent batteries are improperly disposed of, often ending up in landfills, where they pose risks of soil and groundwater contamination due to the leaching of toxic metals and electrolytes.[5–10] In this context, the implementation of organic electrode materials (OEMs) emerges as a promising and more sustainable alternative as they can potentially be synthesized from renewable resources and processed via environmentally benign methods, offering significant potential for reducing the environmental footprint of battery technologies. This includes their application in the design of lithiated organic host materials for positive electrode use,[11] provided that they exhibit a sufficiently high operating potential (i.e., typically above 3.5 V vs. Li^+/Li). However, only a limited number of lithiated organic cathode materials have been reported in the literature, primarily due to the intrinsic challenges associated with their design.[12–14]

For more than a decade, our group has focused particularly on lithiated salts of dihydroxyterephthalate as insertion materials capable of reversibly extracting lithium ions electrochemically, with particular attention to the *para*-regioisomer.[15–19] Our first studied example focused on (2,5-dilithium-oxy)-terephthalate (Li_4-*p*-DHT)[15] as a positive electrode material, for which a two-electron electrochemical storage reaction was theoretically anticipated (Scheme S1). However, experimental results revealed that only one lithium ion could be reversibly deinserted, at an average potential of 2.55 V vs. Li^+/Li, thereby limiting the specific capacity to approximately 120 mAh g^{-1}. This behavior was accompanied by the formation of spin-paired diamagnetic dimers, which contributed to the remarkable stability of the radical state. In a parallel and independent study, Chen's group demonstrated that nanostructuring Li_4-*p*-DHT into nanosheet morphologies via ultrasonic exfoliation allows access to the full capacity.[20] Specifically, these nanosheets, only a few nanometers thick,

delivered an initial discharge capacity of 223 mAh g^{-1} at 0.1 C, approaching the theoretical specific capacity value of 240 mAh g^{-1} for two-electron reaction. Furthermore, this group developed later a Li_4-*p*-DHT/graphene composite that achieved capacities close to 240 mAh g^{-1}, significantly higher than those of most lithiated OEMs.[21] Li_4-*p*-DHT is, however, far from being used in commercial batteries, primarily due to its low average output voltage (~2.6 V vs. Li^+/Li) leading to rapid autoxidation in air.[15] Efforts have been made to increase the working potential by replacing the carboxylate functional groups with more electron-withdrawing groups such as sulfonates,[22] or switching from *para* to *ortho*-regioisomers.[16,18] This strategy involves substituting the two lithium ions that compensate the negative charges of the carboxylate groups in Li_4-*p*-DHT with spectator cations (M^{n+}) of high electronegativity and ionic potential (IP), in order to mitigate the donor inductive effect of the conjugated CO^- and CO_2^- groups. These spectator cations, through their specific coordination environment with the electron-donating phenolate moiety, can modulate the π-electron density within the aromatic ring via the M–O coordination network. This modulation arises from the increased covalent character of the M–O bonds, which alters the electronic structure of the *p*-DHT^{4-} redox active skeleton.[17,23]

We initially investigated and reported the effect of s-block spectator cations in $M^{n+}_{2/n}(Li_2)$-*p*-DHT (M^{n+} = Mg^{2+}, Ca^{2+}, Ba^{2+}) host materials and notably established an empirical correlation between the average operating potential of these materials and the ionic potential (IP) of the spectator cations M^{n+} (assuming an equivalent structural arrangement).[17] We recently extended this empirical correlation to 3d-block elements with the non-redox-active Zn^{2+} cation.[19] In this study, we extend our investigation to transition metals by selecting Cu^{2+} as a representative case. Copper is more electronegative than zinc ($\chi_{AR}(Cu) = 1.75 > \chi_{AR}(Zn) = 1.66$), and as a transition metal, cupric ion possesses a partially filled d-shell that enables it to engage in stronger and more directional M–O coordination bonds.[24] This distinction in electronic structure contributes to the enhanced coordination ability and stronger interaction with electron-donating oxygen ligands. In short, a higher redox potential can be expected than what would be predicted based solely on the empirical correlation with the ionic potential (IP) value. We also demonstrate that the full two-electron electrochemical activity of $Cu(Li_2)$-*p*-DHT can be achieved by promoting its direct growth onto high-surface-area carbon black.

Experimental Section

Chemicals

2,5-dihydroxyterephthalic acid H_4-*p*-DHT (Sigma Aldrich, 98 %), copper(II) bis(trifluoromethane sulfonyl)imide) $Cu(TFSI)_2$ (Solvionic, 99.5 %), lithium methoxide solution MeOLi (Sigma Aldrich, 2.2 molar in methanol), methanol MeOH (Thermo Scientific, 99.9 %), carbon blacks: Ketjenblack EC-600JD (AkzoNobel), C-NERGY SUPER C65 (Imerys) were used without further purification and stored in an argon-filled glovebox.

General characterization techniques

Fourier-transform infrared (FTIR) spectra were acquired using a Bruker Vertex 70 spectrometer within the wavenumber region of 400-4000 cm^{-1} using potassium bromide (KBr) pellets. Pellets were prepared by blending the sample (~1 wt. %) with spectroscopic-grade KBr and compressing the mixture. Powder X-ray diffraction (PXRD) patterns of the samples were recorded in sealed glass capillaries prepared in an Ar-filled glovebox using an INEL XRG3500 diffractometer operating in Debye-Scherrer geometry with Cu-Kα_1 radiation (λ = 1.54060 Å). Both Cu and Li contents were determined by inductively coupled plasma-atomic emission spectroscopy (ICP-AES) using an iCAP 6300 radial analyzer (Thermo Scientific). A monoelement solution of Cu and Li (1000 ppm, CHEMLAB) was used for the calibration. Liquid proton nuclear magnetic resonance (^{1}H NMR) and carbon nuclear magnetic resonance (^{13}C NMR) spectra were obtained with a Bruker Avance IIIHD 500MHz spectrometer, and chemical shifts (δ) were referenced against the solvent signal, specifically set at δ = 2.50 ppm for deuterated dimethyl sulfoxide (DMSO-*d*6) purchased from Eurisotop (purity > 99.9 %). For the derivatization reaction, a few drops of H_2SO_4 were added to the *p*-DHT-based compounds in a sealed NMR sample tube in a glovebox to analyze H_4-p-DHT due to the insolubility of $Cu(Li_2)$-*p*-DHT in anhydrous deuterated solvents preventing its direct characterization. Thermogravimetric analyses coupled with differential scanning calorimetry (TG-DSC) were conducted on powdered samples under an inert argon flow using a SENSYSevo analyzer from Setaram, ramping at 5 °C min^{-1} to a maximum temperature of 800 °C. Scanning electron microscopy (SEM) coupled with Energy Dispersive X-ray Spectroscopy (EDS) was performed with Axia ChemiSEM, ThermoFisher Scientific microscope. (S)TEM data were acquired with a probe corrected ThermoFisher Scientific Themis Z G3 transmission electron microscope (TEM), operating at an acceleration voltage of 300 kV. The microscope was equipped with a SuperX detector (EDS) and a high-resolution energy filter (Gatan GIF Quantum 966 ERS) for Electron Energy-Loss Spectroscopy (EELS). Both the K2 direct electron camera and the US1000 CCD camera were used for high signal-to-noise acquisitions and energy calibration of the spectra, respectively. Since these organic-based samples can be extremely sensitive to

damage from the electron beam and may react with ambient air, a liquid nitrogen-cooling and vacuum-transfer sample holder (from Mel-Build Company) was used. For those samples that had been in contact with the electrolyte, a rinsing step with DMC was performed before drying the powder in vacuum at 90 °C. Inside an argon-filled glovebox, the powders were deposited onto lacey-carbon gold grids, mounted on the sample holder, and examined at –120 °C. To minimize beam-induced damage, spectroscopy measurements were performed using a 2.5 nm probe with a minimum step size of 5 nm, thereby limiting the areal electron dose. EELS spectra were denoised[25] (within Digital Micrograph 3.40), energy calibrated[26] and background subtracted. EELS quantification of Cu, C, and O content was performed within DigitalMicrograph.

Synthesis of the pure Cu(Li_2)-*p*-DHT material

In an argon-filled glovebox, a methanolic suspension of H_4-*p*-DHT (1.0 g, 5.1 mmol, 1 eq.) was prepared by dispersing this diacid in 200 mL of anhydrous MeOH inside a round-bottom flask. Subsequently, 9.3 mL of a MeOLi solution (2.2 M in MeOH, 20.4 mmol, 4 eq.) was added dropwise under continuous stirring, resulting in formation of a clear, homogeneous mixture. After stirring at room temperature for 1 h, powder of $Cu(TFSI)_2$ (3.18 g, 5.1 mmol, 1 eq.) was added to the reaction mixture. The flask was then sealed, heated at 70 °C, and stirred for 16 h. During heating, the initially pale brown precipitate gradually changed to bright brown. After cooling, the solid product was subsequently separated by centrifugation at 6500 rpm for 30 min and washed thoroughly four times with 100 mL of methanol. Following these washing steps, the solid was dried overnight under vacuum at ambient temperature. Finally, the dried material was heated at 110 °C for 16 h under vacuum in a Büchi B-585 glass oven (Kugelrohr drying model) to obtain pure Cu(Li_2)-*p*-DHT as a bright brown-colored powder with an overall yield of ~88 %. Note that the resulting sample formed a dense solid difficult to grind manually. FTIR (cm^{-1}): 1565-1611 ($\bar{\upsilon}_{as}(COO^-)$), 1464-1419 ($\bar{\upsilon}(C=C)$), 1345 ($\bar{\upsilon}_s(COO^-)$), 1215 ($\bar{\upsilon}(C-OLi)$), 895-809 ($\bar{\upsilon}$(C−H tetra-substituted benzene)). ^{1}H NMR (500 MHz, DMSO-d_6 + few drops of H_2SO_4) δ (ppm) = 6.96 (2H, s). ^{13}C NMR (125 MHz, DMSO-d_6 + few drops of H_2SO_4): δ (ppm) = 165.8 (COOH), 147.6 (C−OH), 115.4 (C−COOH), 113.2 (CH). Elemental analysis (calculated, found, wt.%): Cu (23.40 %, 26.12 % ± 0.23), Li (5.11 %, 5.06% ± 0.27).

Synthesis of composite Cu(Li_2)-*p*-DHT/carbon black

The experimental approach consisted of a straightforward adaptation of the synthesis procedure previously described to obtain the pure Cu(Li_2)-*p*-DHT material. In an argon-filed glovebox, a methanolic suspension of H_4-*p*-DHT (1.0 g, 5.1 mmol, 1 eq.) was again prepared by dispersing this diacid in 200 mL of anhydrous MeOH inside a round-bottom flask. Subsequently, Ketjenblack EC-600JD (KB600) (685.2 mg) was added to the suspension and dispersed by stirring for 2 h to ensure an optimized dispersion. Then, MeOLi (2.2 M in MeOH, 20.4 mmol, 4 eq.) was added dropwise. The previously described procedure was rigorously applied without modification. The presence of the porous carbon matrix precluded the use of liquid-state NMR and standard mass-based elemental analysis for characterizing the composite. Instead, ICP-AES analyses performed on concentrated acid-digested samples yielded a Li:Cu molar ratio of approximately 2.03:1. FTIR (cm^{-1}): 1565-1611 ($\bar{\upsilon}_{as}(COO^-)$), 1463-1417 ($\bar{\upsilon}$(C=C)), 1345 ($\bar{\upsilon}_s(COO^-)$), 1215 ($\bar{\upsilon}$(C−OLi)), 895-809 ($\bar{\upsilon}$(C−H tetra-substituted benzene)).

Electrochemical characterization

Electrochemical tests were performed in Swagelok®-type cells, utilizing lithium metal as the counter electrode. A lithium metal disk was used as the negative electrode, with two glass fiber separators (Whatman®) soaked in LP30 electrolyte (1 M $LiPF_6$ dissolved in a 1:1 v/v mixture of ethylene carbonate (EC) and dimethyl carbonate (DMC)). Positive electrodes based on the pure Cu(Li_2)-*p*-DHT material were prepared by manually grinding this active material with 33 wt.% of conductive carbon (Ketjenblack EC-600JD or C-NERGY SUPER C65) together using a mortar and pestle inside an argon-filled glovebox (no binder). The resulting powder mixtures, typically weighing between 5-10 mg, contained about 3-7 mg of Cu(Li_2)-*p*-DHT. Positive electrodes based on Cu(Li_2)-*p*-DHT/KB600 were prepared by manually grinding the as-synthesized material with a mortar and pestle inside an argon-filled glovebox (no binder). Electrochemical measurements were performed using an MPG multichannel system (Bio-Logic S.A., Seyssinet-Pariset, France) at 23 °C.

Protocols for *ex situ* FTIR and ICP-AES analyses

For *ex situ* FTIR and ICP-AES measurements, Swagelok®-type cells were galvanostatically cycled and stopped at selected state-of-charge of interest. The cells were then disassembled inside an argon-filled glovebox. The positive electrodes were carefully removed, rinsed with 30 mL of DMC, and dried under vacuum at 60 °C for 16 h using in a Büchi B-585 glass oven (Kugelrohr drying model). Note that for the cell representing the starting open-circuit potential

(A), the disassembling was performed after ~40 h under open-circuit conditions. For ICP-AES analysis, the dried electrode material was weighed inside an Ar-filled glovebox, then transferred into concentrated nitric acid (18 M HNO_3) and sonicated for 30 min to ensure maximum dissolution of the active material. The resulting suspension was subsequently diluted with ultrapure water to obtain a 6 M HNO_3 solution. Finally, the solution was filtered through a Sartorius Minisart™ NML Syringe Filters (0.65 µm pore size) to remove carbon particles, yielding the final analyte solution.

Results and Discussion

1. Characterizations of Cu(Li_2)-*p*-DHT

The synthesis of the Cu(Li_2)-*p*-DHT compound was directly inspired by that of the recently reported Zn(Li_2)-*p*-DHT,[19] with the sole modification of replacing $Zn(TFSI)_2$ with its commercially available copper counterpart (Scheme S2). The addition of $Cu(TFSI)_2$ to a homogeneous solution of the fully lithiated *p*-DHT ligand in methanol led to the immediate precipitation of a bright brown solid, while the resulting LiTFSI by-product remains in solution and is easily eliminated with a filtration step. Subsequent thermal analysis of the isolated material, after drying at 110 °C under vacuum for 16 h, confirmed by TGA/DSC measurements (Figure S1) that no residual methanol remained within the structure.

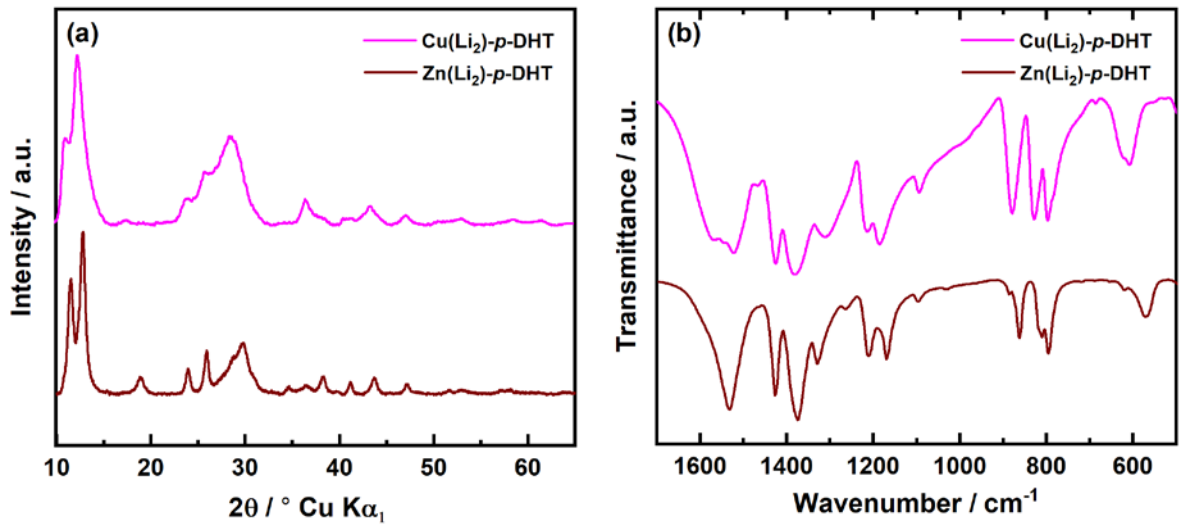

Figure 1. Powder X-ray diffraction patterns and (b) FTIR spectra of Cu(Li_2)-*p*-DHT (magenta) and Zn(Li_2)-*p*-DHT (brown), shown as overlaid plots for comparison.

Figure 1a compares the PXRD patterns collected for Cu(Li_2)-*p*-DHT and Zn(Li_2)-*p*-DHT. The close match in peak positions indicates that Cu(Li_2)-*p*-DHT exhibits also the characteristic lamellar structure typical of this class of compounds, an essential feature for enabling reversible lithium-ion insertion and extraction. However, the noticeably broader peaks observed for Cu(Li_2)-*p*-DHT suggest a reduced crystallite size, likely resulting from differences in nucleation and growth during synthesis. Following the recent determination of the Mg(Li_2)-*p*-DHT crystal structure obtained via a combined approach involving electron diffraction tomography, high-resolution PXRD, and periodical DFT calculations[23]—we extended the structural analysis to the Zn and Cu analogues. Le Bail refinements were successfully carried out to assess the preservation of the lamellar architecture and evaluate variations in unit cell parameters (Figure S2). The slightly expanded cell volumes, compared to the Mg(Li_2)-*p*-DHT phase, may be attributed to the larger ionic radii of Zn^{2+} and Cu^{2+}, which induce subtle lattice distortions.

Similarly, the FTIR spectrum of Cu(Li_2)-*p*-DHT (Figure 1b) exhibit all the characteristic peaks observed for Zn(Li_2)-*p*-DHT, indicating that the substitution does not substantially affect the chemical structure of the material. The position of the asymmetric stretching vibration band of the carboxylate groups ($\bar{\upsilon}_{as}(COO^-)$) serves us as a sensitive indicator of the electron-withdrawing strength imposed by the spectator cation on the *p*-DHT ligand.[17,19] In the case of Cu(Li_2)-*p*-DHT, $\bar{\upsilon}_{as}(COO^-)$ is observed at slightly higher wavenumber compared to the Zn^{2+}, which could be attributed to the slightly higher ionic potential of Cu^{2+} (2.898) relative to Zn^{2+} (2.816) (Table S1). However, comparison with the FTIR spectrum of Mg(Li_2)-*p*-DHT (Figure S3) reveals that the $\bar{\upsilon}_{as}(COO^-)$ band of Cu(Li_2)-*p*-DHT exhibits a similar or slightly greater positive shift relative to Mg(Li_2)-*p*-DHT. Finally, the δ(COO-M) bending vibration in the range of 620-570 cm^{-1} also shows a positive shift for Cu(Li_2)-*p*-DHT, which shows stronger metal-carboxylate interaction than for Zn^{2+}.[27] The shift of the $\bar{\upsilon}$(CO−Li) vibration band could also be used,[19,28] since M^{n+} and an equivalent trend can be found. The interpretation of the position of this infrared vibrational band reaches its limits here, as the observed shifts are minimal, comparable to the subtle differences in terms of IP values between Mg^{2+}, Zn^{2+}, and Cu^{2+}. Nonetheless, a working potential of approximately 3.5 V vs. Li^+/Li can reasonably be anticipated, in line with the values observed for the Mg- and Zn-based phases.

Based on the combined evidence from XRD patterns and FTIR spectra, it can be concluded that the newly synthesized material exhibits a chemical and crystal structure similar to that of Mg(Li_2)-*p*-DHT recently resolved.[23] Additionally, liquid $^1H/^{13}C$ NMR confirmed through derivatization that the organic moiety was unaltered during synthesis (Figure S4) and ICP-AES

analysis confirms the expected stoichiometry of Cu(Li_2)-*p*-DHT by accurately measuring the copper and lithium contents although a slightly higher amount of copper can be noticed (Figure S5).

2. Electrochemical behavior of as-prepared Cu(Li_2)-*p*-DHT in Li half-cell

To assess the electrochemical behavior of Cu(Li_2)-*p*-DHT, galvanostatic cycling tests were performed in Swagelok®-type cells, following a procedure similar to that previously reported for $M^{n+}_{2/n}$(Li_2)-*p*-DHT (M^{n+} = Li^+, Mg^{2+}, Ca^{2+}, Ba^{2+}, Zn^{2+}) using 1 M $LiPF_6$ in EC/DMC (LP30) as the electrolyte, and a typical cycling rate corresponding to the exchange of one Li^+ ion per *p*-DHT^{4-} unit in 5 h.[15,17,19] To ensure consistency with our earlier study on Zn(Li_2)-*p*-DHT, C65 carbon black was selected at this stage.[19] Figure 2a shows the first cycle reported in a potential-composition curve within the 3.0 – 4.0 V vs. Li^+/Li potential range. As previously noted for the zinc-based phase, the cycling profile of Cu(Li_2)-*p*-DHT remains mostly featureless. However, Cu(Li_2)-*p*-DHT shows a significantly lower first discharge capacity of only 56.6 mAh g^{-1}, almost half of the theoretical capacity for one-electron reaction (Scheme S1), together with a markedly higher polarization. Under identical cycling conditions, Zn(Li_2)-*p*-DHT delivers the expected capacity corresponding to a one-electron transfer per *p*-DHT^{4-} unit. This behavior can be attributed to the formation of large aggregates during synthesis, as evidenced by SEM imaging (Figure S6). These aggregates proved difficult to reduce in size through manual grinding, which may hinder both electronic conductivity and lithium-ion transport within the electrode material. The cycling performance of Cu(Li_2)-*p*-DHT, as shown in Figure 2b, demonstrates a relatively stable but modest capacity over 50 cycles. The initial capacity increases a bit over the first 8 cycles before a slight decrease over cycling, stabilizing around 53–55 mAh g^{-1}. The charge capacity follows a similar trend, leading to a coulombic efficiency that quickly rises above 95 % within the first few cycles and remains consistently close to 99 %, indicating good reversibility of the electrochemical process for the considered active part of the Cu(Li_2)-*p*-DHT sample.

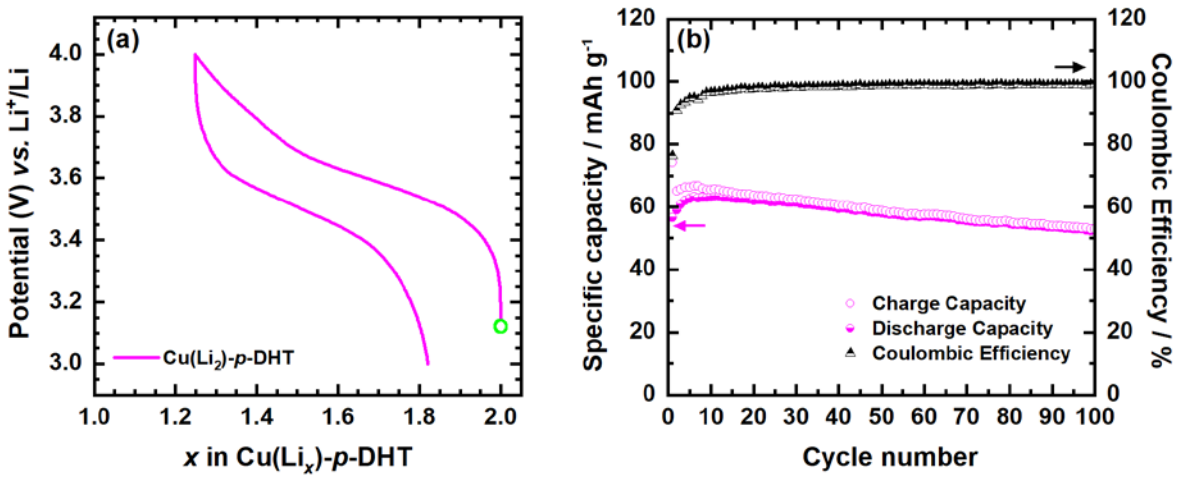

Figure 2. Charge/discharge electrochemical behavior of the Cu(Li_2)-*p*-DHT electrode material mixed with 33 wt% of C65 carbon black measured in Li half-cell and galvanostatically cycled in 1 M $LiPF_6$ in EC/DMC as the electrolyte at a rate of 1 Li^+/5 h. (a) Typical potential-composition trace recorded during the first cycle; the green circle marks the initial open-circuit potential. (b) Corresponding capacity retention and coulombic efficiency upon cycling.

Based on these electrochemical results, it became clear that reducing the particle size was essential to approach the expected theoretical capacity (Q_{1e} = 98.72 mAh g^{-1}) for Cu(Li_2)-*p*-DHT, as achieved with other derivatives previously studied by our group. Consequently, several grinding attempts were carried out. However, the inherent fragility of organic materials prevented the attainment of the desired electrochemical performance through this approach. To overcome this limitation, we explored the *in situ* preparation of a composite electrode by incorporating high-surface-area carbon black directly into the reaction medium during the synthesis of Cu(Li_2)-*p*-DHT in methanol. This carbon-supported organic electrode strategy has been reported several times in the literature,[29,30] employing various types of carbon materials. Such studies were primarily motivated by the fact that most organic electrode materials (OEMs) based on small neutral redox-active molecules suffer from high solubility in organic liquid electrolytes and inherently low electrical conductivity. However, this approach also promotes nucleation on the carbon support at the expense of crystal growth, leading to a carbonaceous material decorated with finely dispersed active material particles.

3. Synthesis and characterization of Cu(Li_2)-*p*-DHT/carbon black composite

Based on a preliminary study, we employed commercially available high-surface-area Ketjenblack EC-600JD (KB600) to prepare the carbon-supported Cu(Li_2)-*p*-DHT electrode, with the objective of achieving a uniform distribution of small Cu(Li_2)-*p*-DHT particles both within and on the surface of the KB600 carbon matrix. Indeed, we experienced that KB600 consistently yielded the most homogeneous dispersion in methanol, without requiring additional processing steps. The experimental procedure, summarized in Figure 3, involved dispersing KB600 into a methanolic suspension of H_4-*p*-DHT, followed by sequential lithiation by acid-base reaction and coordination with Cu^{2+} giving rise to the precipitation of the title compound. SEM images of the resulting Cu(Li_2)-*p*-DHT/KB600 composite reveal a porous morphology, free from large aggregates (Figure S7). By combining EDS mapping (Figure S8), the formation of a homogeneous composite was readily confirmed with Cu(Li_2)-*p*-DHT uniformly deposited onto the carbon support. Furthermore, complementary investigations by both FTIR and PXRD confirmed the formation of Cu(Li_2)-*p*-DHT within the carbon matrix (Figure S9) whereas ICP-AES analyses corroborated the targeted stoichiometry with a Li:Cu molar ratio of 2.03:1.

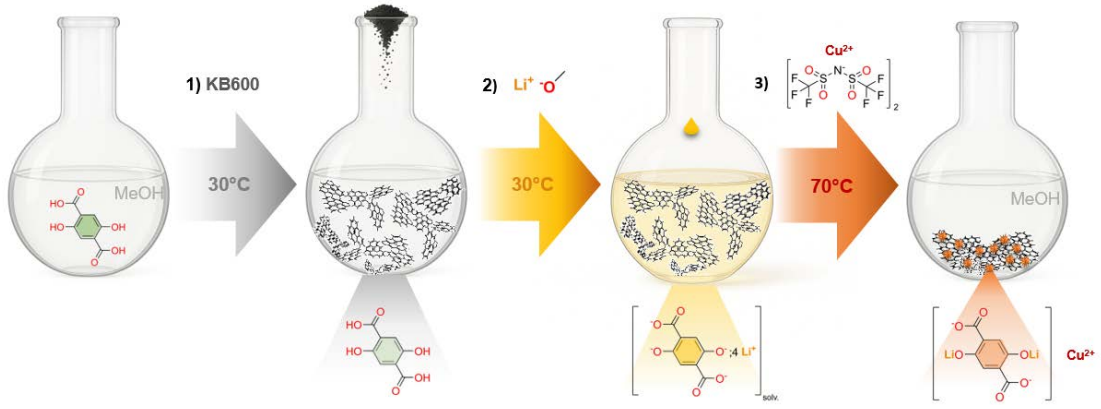

Figure 3. Schematic of the experimental protocol for producing the Cu(Li_2)-*p*-DHT/KB600 composite.

To further advance the characterization, particularly at the nanoscale, a scanning/transmission electron microscopy (STEM) combined with electron energy loss spectroscopy (EELS) was employed. STEM-HAADF imaging also revealed a homogeneous nanoscale mixture of the Cu(Li_2)-*p*-DHT and KB600 particles. Due to the close atomic numbers of the constituent elements, the resulting Z-contrast was found insufficient to distinctly differentiate the two phases within the composite (Figure 4a). High-resolution transmission electron microscopy (HR-TEM) likewise proves inconclusive, as the active material exhibits weak diffraction

contrast, precluding structural delineation. On the other hand, electron energy loss spectroscopy (EELS) offers a robust means of spatially resolving the composite's constituents (Figure S10). As illustrated by the spectrum image in Figure 4b, individual spectra extracted from selected regions (Figure 4c) confirm that the two components are intimately inter-dispersed at the nanometer scale.

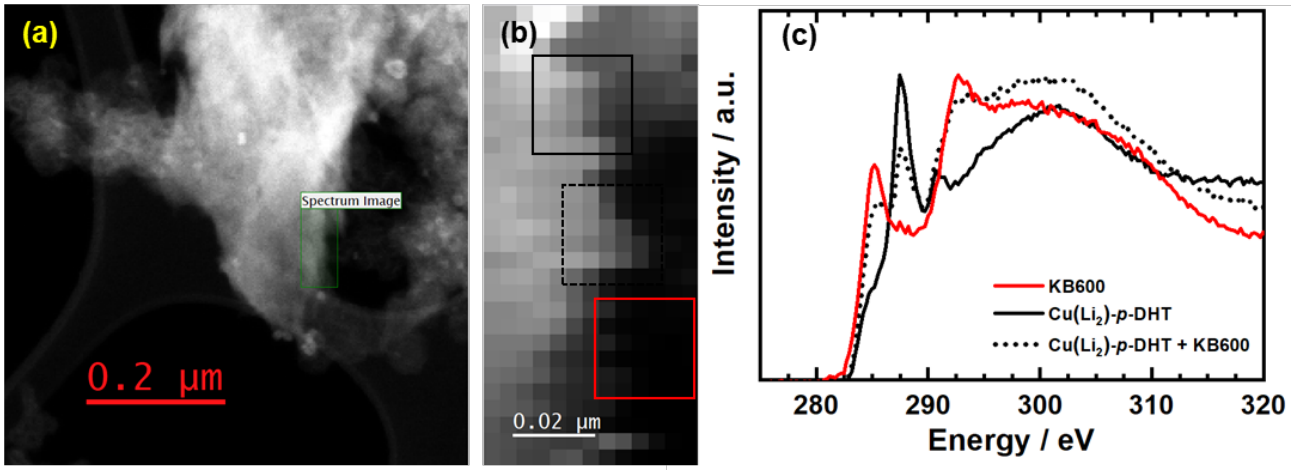

Figure 4. (a) STEM-HAADF image of the Cu(Li_2)-*p*-DHT/KB600 composite. (b) Corresponding spectrum imaging area with squared regions indicating the zones selected for EELS analysis shown in (c). (c) Carbon K-edge spectra extracted from the regions in b): solid black line shows area predominantly containing Cu(Li_2)-*p*-DHT; dotted black line shows area with a mixture of Cu(Li_2)-*p*-DHT and KB600; red line shows area corresponding mainly to KB600 carbon particles.

4. Electrochemical behavior of Cu(Li_2)-*p*-DHT/carbon black composite in Li half-cell and advanced characterizations

The electrochemical performance of the Cu(Li_2)-*p*-DHT/KB600 composite (Figure 5) was evaluated by galvanostatic cycling under identical conditions to those used for the pristine Cu(Li_2)-*p*-DHT mixed with 33 wt.% of C65 carbon black (Figure 2). Unexpectedly, the carbon-supported Cu(Li_2)-*p*-DHT composite electrode initially demonstrates the ability to reversibly extract not only the expected one lithium ion per *p*-DHT^{4-} unit, but also a second one, thereby approaching its full theoretical capacity (Scheme S1). Using our regular experimental conditions, previously reported $M^{n+}_{2/n}$(Li_2)-*p*-DHT (M^{n+} = Li^+, Mg^{2+}, Ca^{2+}, Ba^{2+}, Zn^{2+})[15,17,19] active materials have consistently failed to reach the fully oxidized quinone state. As a result,

the accessible capacity has typically been limited to that corresponding to the extraction of a single lithium ion, even when operating at potentials as high as 4 V vs. Li^+/Li. This unambiguous limitation is attributed to the particular stability of the semiquinone radical state following the one-electron oxidation process, as recently demonstrated in the case of Mg(Li_2)-*p*-DHT.[23] Indeed, the extraction of the second lithium ion in those cases was consistently obstructed by an irreversible Kolbe electrolysis (i.e., an electrochemical decarboxylation reaction occurring typically in the vicinity of 4.0 V vs. Li^+/Li).

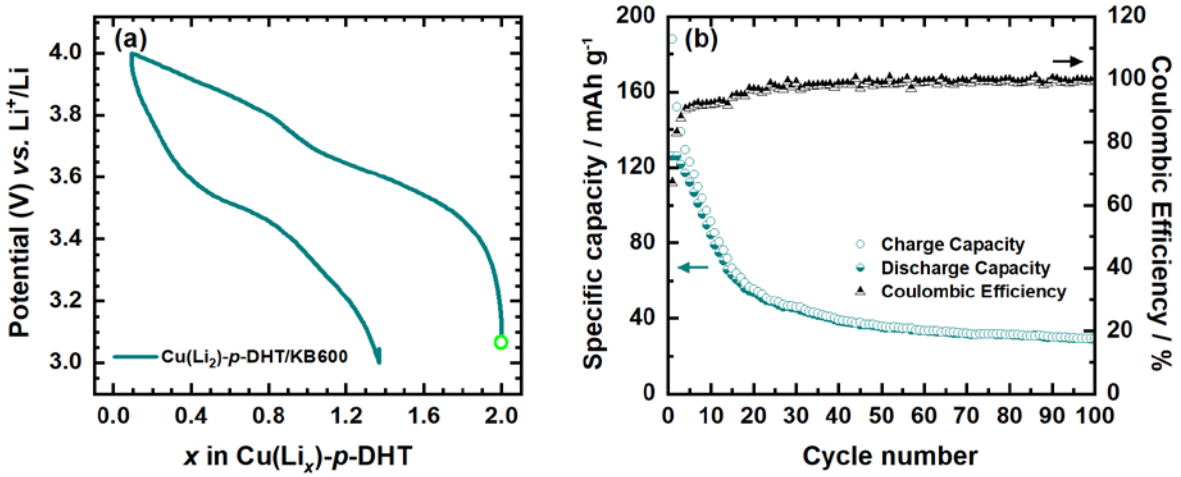

Figure 5. Charge/discharge electrochemical behavior of the Cu(Li_2)-*p*-DHT/KB600 composite electrode (containing 33 wt.% of KB600 carbon) measured in Li half-cell galvanostatically cycled in 1 M $LiPF_6$ in EC/DMC as the electrolyte at a rate of 1 Li^+/5 h (I = 19.7 mA g^{-1}). (a) Typical potential-composition trace recorded during the first cycle; the green circle marks the initial open-circuit potential. (b) Corresponding capacity retention and coulombic efficiency upon cycling.

To provide evidence of a synergistic interaction resulting from the growth of Cu(Li_2)-*p*-DHT on the carbon matrix, complementary cycling tests were performed. Figure S11 shows the typical potential-composition trace recorded during the first cycle with the corresponding capacity retention upon cycling of the Cu(Li_2)-*p*-DHT/KB600 composite alongside that of a manually blended mixture of bulk Cu(Li_2)-*p*-DHT and KB600 carbon. Both samples were prepared with identical carbon content and cycled under the same experimental conditions. The manually blended composite electrode, prepared by simple grinding with a mortar and pestle, exhibited limited specific capacity corresponding to the extraction of less than one lithium ion

per ligand unit. In contrast, the *in situ* synthesized composite delivered an initial charge capacity of approximately 188.2 mAh g^{-1}, approaching the theoretical maximum of 197.4 mAh g^{-1} expected for the extraction of two lithium ions per *p*-DHT^{4-} unit (Scheme S1).

At this stage, it must be pointed out that in bulk Cu(Li_2)-*p*-DHT, extensive intermolecular π–π stacking interactions strongly stabilize the partially oxidized semiquinone intermediate, thereby limiting access to the second electron.[23] In contrast, in the Cu(Li_2)-*p*-DHT/KB600 composite, nanosized Cu(Li_2)-*p*-DHT particles are uniformly dispersed across the high-surface-area KB600 carbon matrix. This effective dispersion, combined with nanoscale-induced effects, likely disrupts the π–π stacking network, thereby facilitating the extraction of the second lithium ion and enabling access to the full two-electron redox process, as previously highlighted by Chen's group with the Li_4-*p*-DHT active material.[20,21] Nevertheless, it is worth noting that achieving the full capacity with the Cu(Li_2)-*p*-DHT/KB600 composite also results in significantly greater capacity fading over subsequent cycles; after 50 cycles together with a markedly higher polarization indicating substantial kinetic limitations (Figure 5). These electrochemical properties differ significantly from those reported by the Chen group for Li_4-*p*-DHT. Surprisingly, in their first study,[20] only the specific capacity increased progressively starting from 140 mAh g^{-1} for the bulk material to 200 mAh g^{-1} for nanoparticles (prepared by ball-milling), and up to 225 mAh g^{-1} corresponding to the full two-electron reaction, without any change in terms of cycle profile, average operating potential, polarization while maintaining excellent cycling stability. The detailed reasons behind this rapid capacity fade with the Cu(Li_2)-*p*-DHT/KB600 composite will be elucidated further later in the article through *ex situ* characterizations and analysis.

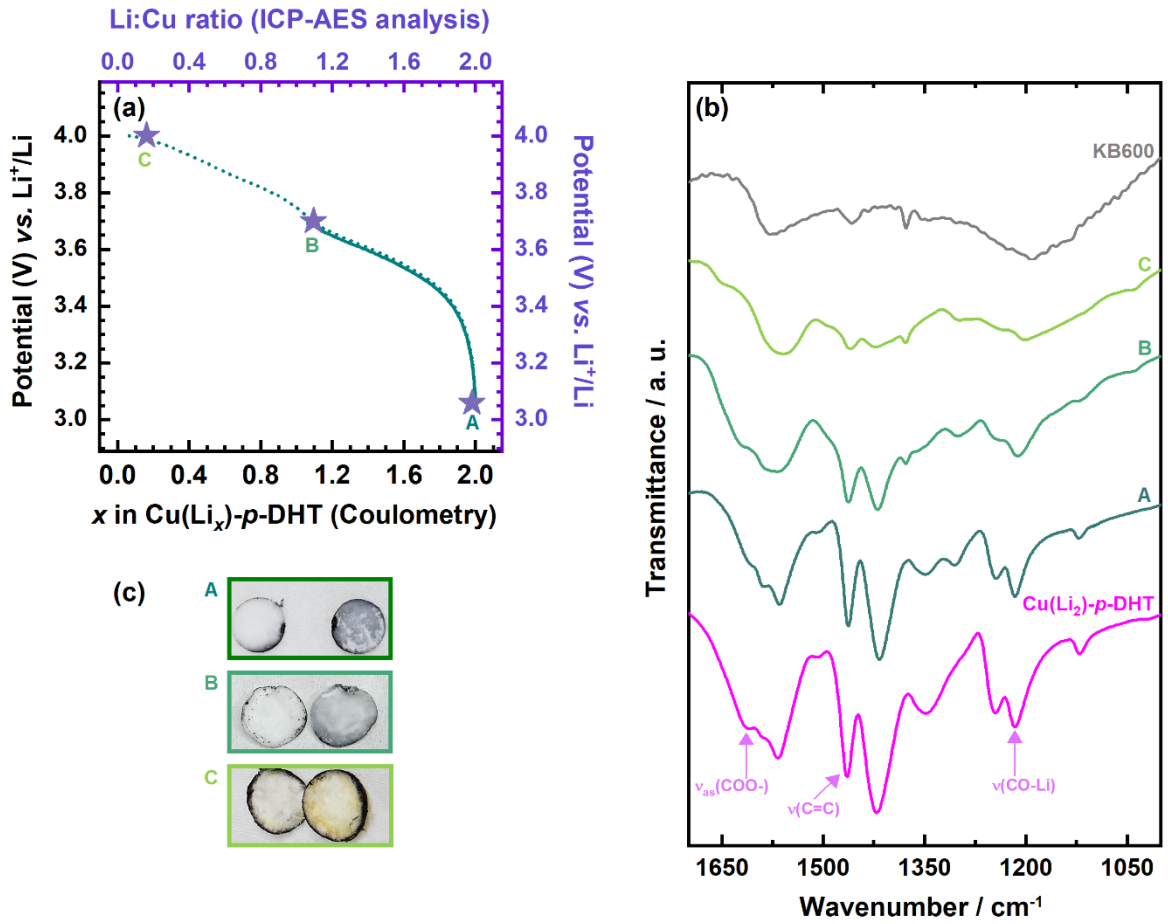

Figure 6. (a) Potential-composition trace of the Cu(Li$_2$)-*p*-DHT/KB600 composite obtained during galvanostatic cycling in LP30 electrolyte at a rate of 1 Li^+/20 h. The bottom x-axis denotes the calculated lithium-ion stoichiometry (moles of Li^+ per formula unit of Cu(Li$_x$)-*p*-DHT) based on coulometry measurements, whereas the top x-axis indicates lithium content quantified through ICP-AES measurements. Electrochemical traces are shown in cyan. Points A, B, and C correspond to the states selected for *ex situ* analyses at OCV (A), 3.7 V (B), and 4.0 V (C) vs. Li^+/Li. (b) Overlaid FTIR spectra of pristine Cu(Li$_2$)-*p*-DHT powder (magenta), KB600 carbon sample (gray), and Cu(Li$_2$)-*p*-DHT/KB600 electrodes collected at states A, B, and C (green). (c) Images of separators recovered from the cells at initial state A, B (3.7 V), and C (4.0 V).

To confirm that the additional capacity arises from the participation of a second lithium ion in Cu(Li$_2$)-*p*-DHT particles, we conducted an *ex situ* study by combining first ICP-AES and FTIR analyses based on the characterization of the positive electrode during the first charge by selecting 3 representative states-of-charge (Figure 6): points labeled A, B, and C corresponding

to the initial state, the middle charged state at 3.7 V (one-electron oxidation), and finally the full charged state at 4.0 V vs. Li^+/Li (two-electron oxidation).

ICP-AES measurements performed on samples charged to 3.7 V (B) and 4.0 V (C) revealed Li:Cu atomic ratios of 1.09:1 and 0.16:1, respectively (Figure 6b), thereby confirming unambiguously the progressive and almost full extraction of lithium ions from the host material. This compositional shift was supported by FTIR analyses (Figure 6a), where the gradual change and disappearance of the $\bar{\upsilon}$(CO−Li) stretching vibration around 1214 cm^{-1} confirm partial and then complete delithiation of the phenolic sites at 3.7 V and 4.0 V, respectively. Concurrently, the loss of the characteristic aromatic $\bar{\upsilon}$(C=C) (1464-1419 cm^{-1}) stretching band at the end of the first charge cycle indicates the loss of aromaticity, accompanied by the formation of a quinonoid carbonyl structure. This structural evolution is further confirmed by broad peaks in the 1560-1650 cm^{-1} region, corresponding to $\bar{\upsilon}$(C=O) stretching modes and $\bar{\upsilon}$(C=C) stretching vibrations of the quinone rings.[31–37] Notably, these carbonyl signals exhibit downshift and spectral broadening in the presence of KB600 carbon, consistent with previously reported π-π interactions between quinone-based organic moieties and graphitic surfaces.[38] Also, in these particular spectra, there is a significant contribution from the KB600 background. Correlating the FTIR data with the potential-composition curve clearly indicates that the extraction of the first lithium ion occurs within the 3.4-3.7 V vs. Li^+/Li potential range, consistent with the behavior of the bulk Cu(Li_2)-*p*-DHT, and corresponds to the formation of the semi-quinone radical state as illustrated in Scheme S1. In the case of the Cu(Li_2)-*p*-DHT/KB600 composite, however, lithium extraction proceeds beyond one lithium, approaching a two-lithium process and leading to the formation of the fully quinone form at 4.0 V (C). Notably, at potentials above 3.9 V, the separators exhibit a brown coloration, consistent with the increased solubility of the copper 1,4-benzoquinone-2,5-dicarboxylate. This latter retains only two delocalized negative charges on its molecular backbone, in contrast to Cu(Li_2)-*p*-DHT or Cu(Li_1)-*p*-DHT$^{\bullet}$, as thoroughly discussed in our earlier studies on organic host materials.[11,39–41]

For more detailed nanoscale analysis, STEM combined with EELS was again employed. The EELS spectra corresponding to the Cu(Li_2)-*p*-DHT consistently show three well-separated peaks at 285.0(1) eV, 287.7(1) eV, and 291.0(1) eV (Figure 7). The interpretation of the fine structure at the carbon K-edge can be reliably based on the presence of three distinct types of carbon bonding in the pristine Cu(Li_2)-*p*-DHT. This supports the assignment of the lowest-energy peak (most reduced carbon) to aromatic carbons, the middle peak to phenolic carbons,

and the highest-energy peak at 291.0 eV to carboxylate groups. This peak assignment is consistent with prior literature based on EELS and near-edge X-ray absorption fine structure spectroscopy (NEXAFS) of carbon-based materials.[42,43] Unfortunately, the relative intensities of the peaks cannot be directly correlated to the number of equivalent atoms without EELS spectral simulations, which would be necessary for quantitative interpretation.

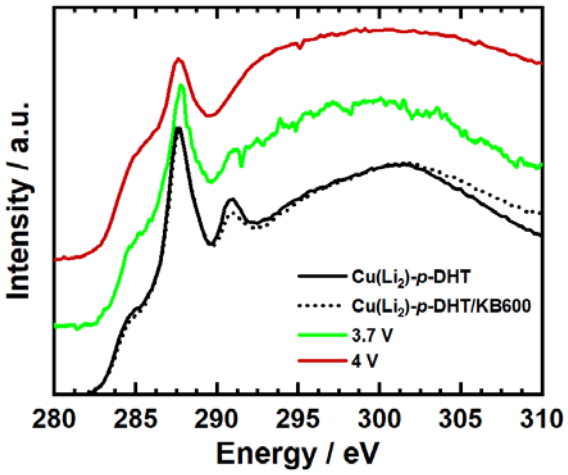

Figure 7. EELS carbon K-edge spectra of pristine Cu(Li$_2$)-*p*-DHT (solid black line), the Cu(Li$_2$)-*p*-DHT/KB600 composite (dotted black line), and the Cu(Li$_2$)-*p*-DHT/KB600 composite after charging to 3.7 V (green) and 4.0 V (red) vs. Li^+/Li, respectively.

The spectrum obtained from material recovered from a battery charged to 4.0 V (C) differs significantly from that of the pristine Cu(Li$_2$)-*p*-DHT. The most prominent change in the spectrum is a decrease in the maximum intensity associated with a broadening of the 287.7 eV peak, attributed to phenolic groups, which are involved in the redox process. While more difficult to interpret, the redistribution of spectral weight toward lower energies in the 292–305 eV range between the pristine and 4.0 V states suggests significant changes in bond lengths and electronic density, likely associated with the oxidation-induced formation of quinoid structures. In the case of the intermediate state-of-charge at 3.7 V (B), the spectrum appears to lie between those of the pristine and the recovered sample at 4.0 V (C). This intermediate character is consistent with partial oxidation to the semi-quinone radical state, and no anomalous features indicative of unexpected electronic configurations are observed. The oxygen K-edge spectra of both the pristine and the fully oxidized materials (C) exhibit a major peak at 533.9(1) eV with a minor shoulder at 531.5(2) eV. However, assigning these features

to specific types of oxygen atoms is too uncertain to elaborate further on (Figure S12). As with the carbon K-edge, the oxygen spectra show a systematic shift of spectral weight toward lower energies in the 537–552 eV range upon oxidation. Elemental quantification performed by both EDX and EELS yielded values consistent with the expected stoichiometry. However, due to the low copper content (<5 at.%), the associated error for Cu quantification was large (exceeding the typical 10-20 % uncertainty for EELS). The fine structure of the Cu $L_{2,3}$-edge is consistent with a Cu^{II} oxidation state, although the low signal makes precise determination difficult (Figure S13). Lithium content was not quantified by EELS due to its low concentration (<10 at.%).

In summary, EELS analyses confirms that the full state-of-charge (oxidation to 4.0 V) induces pronounced changes in carbon electronic structures, consistent with the conversion of phenolate groups to quinoid species and the associated complete loss of phenolic character. The intermediate spectrum at 3.7 V (B) reflects the formation of a semi-quinone radical state. These spectroscopic signatures align with FTIR and electrochemical data, collectively supporting a gradual two-step lithium extraction.

Finally, it was found relevant to extend our investigation to the subsequent discharge (Figure S14). The collected FTIR spectra of the recovered positive electrodes post-discharge at 3 V after charging up to 3.7 V (D) and 4.0 V (E) vs. Li^+/Li, respectively, are shown in Figure S14b. For the latter state-of-charge points, the $\bar{\upsilon}$(CO−Li) stretching vibration and aromatic $\bar{\upsilon}$(C=C) stretching band are completely recovered, indicating re-insertion of lithium ions and the regain of the aromaticity of the ring. The corresponding potential versus composition plot, Figure S14a, suggests that charging till 4.0 V enables the extraction of two lithium ions out of the Cu(Li_2)-*p*-DHT, but it is poorly reversed during discharge. As previously highlighted, the formation of copper 1,4-benzoquinone-2,5-dicarboxylate in the fully charged state reduces the number of delocalized negative charges within the ligand. This, in turn, enhances its solubility in carbonate-based liquid electrolytes and causing rapid capacity fade. This issue is effectively mitigated when the upper cut-off potential is limited to 3.7 V, corresponding to Cu(Li_2)-*p*-DHT/Cu(Li_1)-*p*-$DHT^{\bullet}$ one-electron reaction, under which the electrochemical reaction proceeds reversibly with excellent cycling stability (Figure 8) like our formerly studied $M^{n+}_{2/n}$(Li_2)-*p*-DHT (M^{n+} = Li^+, Mg^{2+}, Ca^{2+}, Ba^{2+}, Zn^{2+}) active materials.[15,17,19] This controlled redox pathway enables stable cycling with negligible capacity loss and no visible electrolyte discoloration. An initial discharge capacity of 75.3 mAh g^{-1} is delivered, with

96% of the capacity retained after 50 cycles and a coulombic efficiency of 99.4 %; the carbon matrix enabling quite low overpotentials both in charge and in discharge (Figure S14a). When cycled at the higher rate of 1 Li^+ exchanged in 5 hours (19.7 mA g^{-1}), 400 cycles were recorded despite a slightly lower stability (Figure S15). The initial discharge capacity of 69.0 mAh g^{-1} increased to 72.8 mAh g^{-1} at the 6th cycle before gradually decreasing to 53.5 mAh g^{-1} at the 400th cycle with an average coulombic efficiency of 98.3 %.

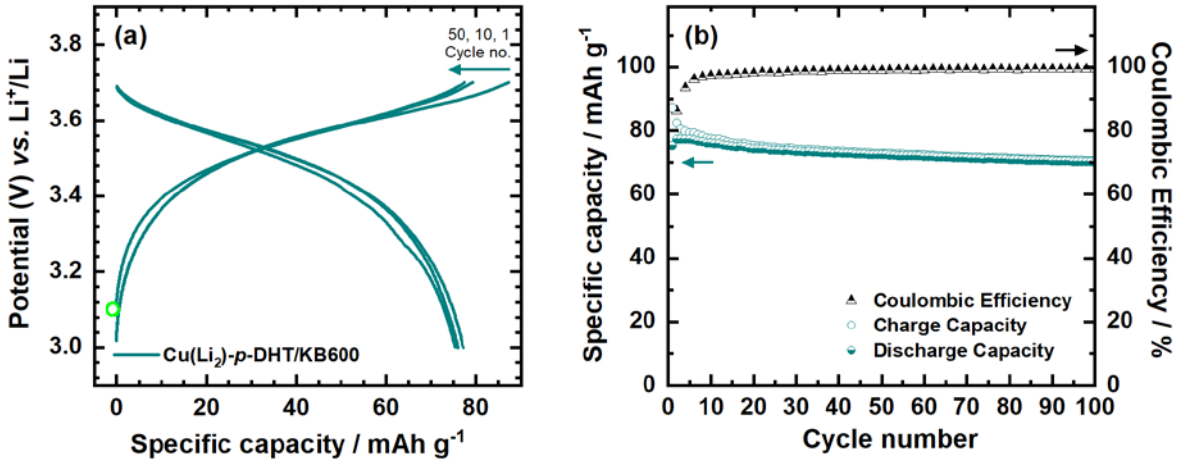

Figure 8. Charge/discharge electrochemical behavior of the Cu(Li_2)-*p*-DHT/KB600 carbon composite electrode (containing 33 wt% of KB600 carbon) measured in Li half-cell galvanostatically cycled in 1 M $LiPF_6$ in EC/DMC as the electrolyte at a rate of 1 Li^+/20 h (I = 4.9 mA g^{-1}). (a) Typical potential-specific capacity trace for cycle no. 1, 10, and 50; the green circle marks the initial open-circuit potential. (b) Corresponding capacity retention and coulombic efficiency upon cycling.

Conclusion

In this study, we report the synthesis of a novel lamellar lithiated organic cathode material, Cu(Li_2)-*p*-DHT belonging to our formerly studied $M^{n+}_{2/n}(Li_2)$-*p*-DHT (M^{n+} = Li^+, Mg^{2+}, Ca^{2+}, Ba^{2+}, Zn^{2+}) family of active host materials. In its initial form, the material displayed limited electrochemical performance, extracting fewer than one lithium ion per *p*-DHT^{4-} unit, which was attributed to reduced reactivity caused by large particle aggregates and associated size effects. To address these kinetic limitations, we developed a carbon composite of Cu(Li_2)-*p*-DHT using high-surface-area conductive carbon (KB600), following the established strategy of carbon-supported organic electrode materials (OEMs). Unexpectedly, this approach led to the

successful extraction of the second lithium ion giving rise to the full theoretical capacity. This is the first report of complete two-electron electroactivity in the M(Li_2)-*p*-DHT-based lamellar system excluding M^{n+} = Li^+, formerly reported by Chen's group.[20,21] However, the extraction of the second lithium ion gives rise to anticipated challenges associated with the reduction of the ligand's overall delocalized anionic charge (from a tetranionic to a dianionic organic backbone), which enhances the solubility of the active material in the fully charged state (quinone form) when using organic liquid electrolytes. Consequently, the system exhibits poor electrochemical performance upon cycling, characterized by pronounced polarization. These results set a new benchmark within the M(Li_2)-*p*-DHT series and offer valuable insights for advancing sustainable, high-performance organic lithium-ion batteries by reengineering organic host materials at both the molecular and solid-state scales.

Supporting Information

The authors have cited additional references within the Supporting Information.

Acknowledgements

All transmission electron microscopy measurements were carried out with the Nant'Themis, part of IMN's characterization platform, PLASSMAT, Nantes, France. DB acknowledges STandUP for Energy. As a part of the DESTINY PhD program, this publication is acknowledged by funding from the European Union's Horizon2020 research and innovation program under the Marie Skłodowska-Curie Actions COFUND (Grant Agreement #945357). This work includes NMR experiments carried out on the CEISAM NMR platform, Nantes Université. Both Li and Cu contents were determined by ICP-AES analyses performed at the LPG-UMR 6112 (C. La, M. Rivoal), Nantes Université. We are deeply grateful to Y. Fretel and E. Quarez for their complementary support in the experimental work.

Keywords: Organic electrode materials • Lithiated organic cathode • Carbon-supported organic electrodes • Carboxyphenolate

References

[1] T. Kim, J. Park, S. K. Chang, S. Choi, J. H. Ryu, H. Song, *Advanced Energy Materials* **2012**, *2*, 860–872.

[2] J. B. Goodenough, *Energy Environ. Sci.* **2014**, *7*, 14–18.

[3] G. E. Blomgren, *J. Electrochem. Soc.* **2017**, *164*, A5019–A5025.

[4] M. Li, J. Lu, Z. Chen, K. Amine, *Advanced Materials* **2018**, *30*, 1800561.

[5] P. Poizot, J. Gaubicher, S. Renault, L. Dubois, Y. Liang, Y. Yao, *Chem. Rev.* **2020**, *120*, 6490–6557.

[6] P. Meshram, A. Mishra, Abhilash, R. Sahu, *Chemosphere* **2020**, *242*, 125291.

[7] Y. Bai, N. Muralidharan, Y.-K. Sun, S. Passerini, M. Stanley Whittingham, I. Belharouak, *Materials Today* **2020**, *41*, 304–315.

[8] E. Fan, L. Li, Z. Wang, J. Lin, Y. Huang, Y. Yao, R. Chen, F. Wu, *Chem. Rev.* **2020**, *120*, 7020–7063.

[9] W. Mrozik, M. Ali Rajaeifar, O. Heidrich, P. Christensen, *Energy & Environmental Science* **2021**, *14*, 6099–6121.

[10] K. M. Winslow, S. J. Laux, T. G. Townsend, *Resources, Conservation and Recycling* **2018**, *129*, 263–277.

[11] P. Poizot, F. Dolhem, *Energy Environ. Sci.* **2011**, *4*, 2003–2019.

[12] Y. Lu, Q. Zhang, F. Li, J. Chen, *Angew Chem Int Ed* **2023**, *62*, e202216047.

[13] X. Guo, P. Apostol, X. Zhou, J. Wang, X. Lin, D. Rambabu, M. Du, S. Er, A. Vlad, *Energy Environ. Sci.* **2024**, *17*, 173–182.

[14] A. E. Lakraychi, I. E. Udom, W. Ren, Y. Yao, *ChemSusChem* **2025**, 2402779.

[15] S. Renault, S. Gottis, A.-L. Barrès, M. Courty, O. Chauvet, F. Dolhem, P. Poizot, *Energy Environ. Sci.* **2013**, *6*, 2124–2133.

[16] S. Gottis, A.-L. Barrès, F. Dolhem, P. Poizot, *ACS Appl. Mater. Interfaces* **2014**, *6*, 10870–10876.

[17] A. Jouhara, N. Dupré, A.-C. Gaillot, D. Guyomard, F. Dolhem, P. Poizot, *Nat Commun* **2018**, *9*, 4401.

[18] L. Bernard, A. Jouhara, E. Quarez, Y. Levieux-Souid, S. Le Caër, P. Tran-Van, S. Renault, P. Poizot, *Inorganics* **2022**, *10*, 62.

[19] A. Shyma Sajeevan, L. Bernard, P. Tran-Van, D. Brandell, S. Renault, P. Poizot, *ACS Appl. Polym. Mater.* **2024**, *6*, 10102–10112.

[20] S. Wang, L. Wang, K. Zhang, Z. Zhu, Z. Tao, J. Chen, *Nano Lett.* **2013**, *13*, 4404–4409.

[21] Q. Zhao, J. Wang, C. Chen, T. Ma, J. Chen, *Nano Res.* **2017**, *10*, 4245–4255.

[22] A. E. Lakraychi, E. Deunf, K. Fahsi, P. Jimenez, J.-P. Bonnet, F. Djedaini-Pilard, M. Bécuwe, P. Poizot, F. Dolhem, *J. Mater. Chem. A* **2018**, *6*, 19182–19189.

[23] A. Jouhara, E. Quarez, N. Gautier, F. Boucher, E. Janod, N. Dupré, J. Gaubicher, P. Poizot, *accepted* **2025**.

[24] D. Chapman, *Nature* **1954**, *174*, 887–888.

[25] G. Lucas, P. Burdet, M. Cantoni, C. Hébert, *Micron* **2013**, *52–53*, 49–56.

[26] P. Abellan, E. Gautron, J. A. LaVerne, *J. Phys. Chem. C* **2023**, *127*, 15336–15345.

[27] S. Bette, R. K. Kremer, G. Eggert, R. E. Dinnebier, *Dalton Transactions* **2018**, *47*, 8209–8220.

[28] L. Sieuw, A. E. Lakraychi, D. Rambabu, K. Robeyns, A. Jouhara, G. Borodi, C. Morari, P. Poizot, A. Vlad, *Chem. Mater.* **2020**, *32*, 9996–10006.

[29] Z. Zhu, J. Chen, *J. Electrochem. Soc.* **2015**, *162*, A2393.

[30] S. Renault, D. Brandell, T. Gustafsson, K. Edström, *Chem. Commun.* **2013**, *49*, 1945.

[31] X. Gao, Y. Wang, L. T. Menezes, Z. Huang, H. Kleinke, Y. Li, *Advanced Functional Materials* **2024**, *34*, 2315669.

[32] K. Pirnat, R. Dominko, R. Cerc-Korosec, G. Mali, B. Genorio, M. Gaberscek, *Journal of Power Sources* **2012**, *199*, 308–314.

[33] G. Ma, Z. Ju, Y. Chen, R. Wang, Z. Yuan, H. Du, M. Cai, M. Gao, Y. Wang, G. Yu, *Chem. Sci.* **2025**, *16*, 5986–5994.

[34] J. D. Cyran, J. M. Nite, A. T. Krummel, *J. Phys. Chem. B* **2015**, *119*, 8917–8925.

[35] N. M. Khamaletdinova, I. N. Meshcheryakova, A. V. Piskunov, O. V. Kuznetsova, *J Struct Chem* **2015**, *56*, 233–242.

[36] Z. Lin, H.-Y. Shi, L. Lin, X. Yang, W. Wu, X. Sun, *Nat Commun* **2021**, *12*, 4424.

[37] M. Nonella, G. Mathias, P. Tavan, *J. Phys. Chem. A* **2003**, *107*, 8638–8647.

[38] K. Molčanov, B. Kojić-Prodić, *IUCrJ* **2019**, *6*, 156–166.

[39] H. Chen, M. Armand, G. Demailly, F. Dolhem, P. Poizot, J. Tarascon, *ChemSusChem* **2008**, *1*, 348–355.

[40] M. Armand, S. Grugeon, H. Vezin, S. Laruelle, P. Ribière, P. Poizot, J.-M. Tarascon, *Nature Mater* **2009**, *8*, 120–125.

[41] H. Chen, M. Armand, M. Courty, M. Jiang, C. P. Grey, F. Dolhem, J.-M. Tarascon, P. Poizot, *J. Am. Chem. Soc.* **2009**, *131*, 8984–8988.

[42] A. Braun, F. E. Huggins, N. Shah, Y. Chen, S. Wirick, S. B. Mun, C. Jacobsen, G. P. Huffman, *Carbon* **2005**, *43*, 117–124.

[43] G. D. Cody, H. Ade, S. Wirick, G. D. Mitchell, A. Davis, *Organic Geochemistry* **1998**, *28*, DOI 10.1016/S0146-6380(98)00010-2.

Entry for the Table of Contents

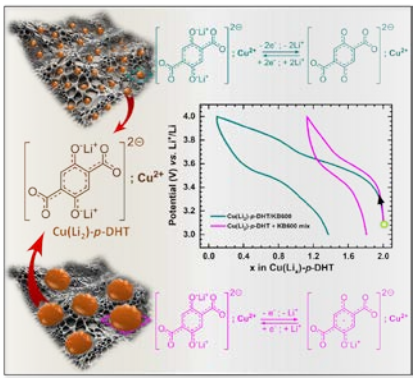

Achieving full two-electron electrochemical activity in Cu(Li_2)-*p*-DHT (copper(II) (2,5-dilithium-oxy)-terephthalate) via *in situ* growth on high-surface-area carbon black. While the electrode delivers high capacity, the solubility of the oxidized quinone species hinders long-term cycling stability.